# Technical Note

# Numerical Estimation of Film Thickness
# With an Air-Assisted Spray Gun

Yusuf Mert BAYTOK[1)*], Aytunç EREK[1)], Orçun SAF[2)]

[1)] *Department of Mechanical Engineering, Dokuz Eylül University*
İzmir, Turkey

[2)] *Standard Profil Automotive*
Manisa, Turkey

*Corresponding Author e-mail: baytok.yusufmert@ogr.deu.edu.tr

The main goal of this study is to present the effects of spraying parameters on the numerical evaluations of the fundamental behaviors of an air-assisted spray gun during the formation of child droplets in the spray flow field and material deposition on the target surface. For this purpose, first of all, the air-assisted spray gun geometry was created using the Solidworks software. Then, a computational domain with a 3D, unstructured grid structure was generated using the ANSYS-Workbench meshing tool. Numerical calculations were conducted using ANSYS-Fluent 2020-R2 commercial software. Different breakup models and their effects on the child droplet size were investigated. By coupling the Taylor analogy breakup (TAB) model and discrete phase model (DPM), the droplet size, trajectory, and coating thickness calculations were made under different atomizing air pressures. Also, the effects of spraying distance and droplet size on coating thickness and the critical Weber (We) number on the atomized particle diameter and particle speed were investigated. The results show that with the increase in atomizing air pressure, droplet sizes decrease and the film thickness on the center of the target surface and droplet speeds increases. Also, increasing the critical Weber number makes it more difficult to atomize the droplets.

**Keywords:** air-assisted spray gun; film thickness; discrete phase model (DPM); breakup.

## 1. Introduction

Air-assisted pneumatic spray guns are widely used in industry to apply coating material to the target surfaces of different geometries. During the coating process, paint or coating liquid is sprayed off and deposited on the target surface. The perceived quality of the products can be directly influenced by the quality of the surfaces. A coating is applied to the material in order to prevent sticking due to friction on the part under the influence of force, for example, in automotive sealing profiles. On the other hand, the coating material pene-

trates pits and scratches due to the strong impact momentum of the droplets, boosting corrosion protection quality. Achieving consistently high-quality coating surfaces depends on environmental factors such as temperature, pressure, relative humidity, spatial location, the geometry of the spray gun, nozzle outlet pressure values, mass flow rate and viscosity of the coating material [1]. The sprayed area and the thickness of the coating layer are the main concerns in the process. Besides, creating a coating deposition model and planning the trajectory of the spray gun remains a difficult problem to solve. Improper coating deposition model and spray gun trajectory calculations will reduce the uniformity of the coating film and the quality of the product. Further, it affects the transfer efficiency (the proportion of sprayed mass to deposited mass) [2]. In this sense, it is important to understand the droplet breakup mechanism to increase process controllability.

Atomization is the process of separating a large number of droplets from a bulk liquid and dispersing them in a gaseous phase [3]. The spray coating process first involves primary and secondary atomization of the coating material and then spraying the coating material onto the surface to be coated. The coating material consists of a certain amount of liquid and solid content. As the liquid evaporates, only the solid content eventually remains on the coating surface [4]. Many studies have employed computational fluid dynamics (CFD)-based approaches to simulate coating thickness distribution since the introduction and widespread application of CFD technology. The coating process is described as a two-phase gas-liquid flow using a CFD-based technique.

In recent years, many experimental and numerical studies have been carried out [3–13]. CHEN *et al.* [5] proposed a mathematical model to evenly distribute the painting material. They arranged tool velocity and tool height to optimize the distribution. KIM *et al.* used the Gaussian model and surface mapping technique for a painting deposition model [6]. LUANKULARB *et al.* [7] investigated the effects of input parameters such as spray time, nozzle size, and pressure on material consumption and dry film thickness by developing a linear regression model. FOGLIATI *et al.* [8] analyzed the spray deposition mechanism by using the volume of fluid (VOF) method to track the free surface. By this method, they obtained initial conditions outside of the nozzle. However, this method is highly mesh dependent and requires high computational cost as the length scales change abruptly. YE *et al.* [9–10] used an experimental-based method to define droplet velocity and diameter distribution below a certain distance of the spray gun nozzle by using laser Doppler anemometry (LDA). Next, using the Euler-Lagrangian approach, they injected experimental data into a continuous phase to solve the flow field and determine film thickness on the target surface. XIE and WANG [11] directly injected the droplet phase data into the flow field from the outlet of the spray gun nozzle. They considered the influence of shaping

air on the flow field. WANG *et al.* [12] investigated the influence of spray gun geometry on the flow field and coating film thickness.

In this paper, the DPM and different secondary breakup models such as TAB, Kelvin-Helmoltz-Rayleigh-Taylor (KHRT), and stochastic secondary droplet (SSD) models are applied to the droplet to predict secondary breakup and determine child droplet size distribution. The two-phase spray flow is described using the Euler-Lagrange method. The influence of the assisting air pressure on the airflow field and the coating thickness distribution by variating the air pressure, the distribution of the film thicknesses according to different particle diameters, variation of film thickness and particle velocity according to distance are studied. To validate the numerical work, the results are compared with the numerical and experimental results in the planar vertical case in reference [11].

## 2. MATHEMATICAL BACKGROUND

During spraying, there is a velocity difference between the liquid phase and the sprayed air. After the primary and secondary breakup, the liquid phase generates tiny droplets that are transported by air to the surface of the workpiece to create a liquid film under the effect of an air shock.

In general, two distinct techniques for multiphase modeling have been proposed [13]. All phases are regarded as fluids in the Eulerian model, obeying one-phase equations of motion and appropriate boundary conditions set at phase boundaries. Using an averaging approach, the flow equations are obtained from these equations of motion. There are numerous ways to carry out this average procedure, including time averaging, volume averaging, and ensemble averaging, or perhaps a mixture of these fundamental techniques [14]. In the Lagrangian approach, the fluid is treated as continuum phase, while the motion of the particulate phase is obtained by integrating the equation of motion of individual particles along their trajectories. One result of such complexity related to multiphase flows is that the dynamics of these flows is still a branch of experimental fluid dynamics. Yet, trial and error testing is the only key for many multiphase flow engineering problems, especially in small-scale models. In general, the advantage of the Eulerian approach is that it can be applied to any multiphase flow, regardless of the number and nature of the phases. On the other hand, the disadvantage of this model is that most of the time it leads to a complex sets of flow equations and closure conditions. In some applications, such as for a relatively homogeneous suspension of dispersed phases that follows the motion of the continuous phase, it is possible to use the so-called mixture model, a simplified formulation of the Eulerian approach. The mixture model includes the conservation equations of the mixture as well as continuity equations for each dispersed phase [14].

### 2.1. Discrete phase model (DPM)

Atomization occurs due to the effect of high-speed air flow coming through spray gun nozzles. The broken-up particles interact with the target surface after being broken up by the airflow. The airflow field and droplets can be considered a two-phase liquid-gas flow field. In this study, to simulate the spraying process, DPM, a multiphase method based on the Euler-Lagrange approach, is used. The continuous phase (air phase) is calculated in the Euler coordinate frame, while the discrete phase (droplet phase) is calculated in the Lagrange coordinate frame. The flow field of the gas phase is governed by the fundamental conservation law, notably the continuity and momentum equations, which are crucial in the spray painting process. By integrating the discrete phase equation of motion in the Lagrange coordinate system, the droplet trajectories are computed as follows:

$$(2.1) \qquad \frac{\mathrm{d}u_P}{\mathrm{d}t} = F_D\,(u - u_D) + F_G,$$

where $u_P$ is the droplet velocity, $F_D\,(u - u_D)$ is the drag force per unit particle mass, $u$ is the instantaneous, continuous phase (air phase) velocity obtained by adding the effects of the local mean velocity and the fluctuating velocity caused by turbulence, and $F_G$ is the gravitational force per unit particle mass. The equation of motion is derived from a force balance on the particle. Since droplet density is much more higher than air density, and the volume fraction of the liquid is less than 1%, virtual mass force and Saftman lift force may be neglected. Because the mass flow rate of paint is quite low, the interaction between particles may be disregarded.

### 2.2. Wall liquid film model

After atomization occurs, droplets are transported to the target surface and create a liquid film. The liquid film creation process uses the wall surface liquid film model to forecast the liquid film formed after the liquid phase accumulates on the workpiece's surface and the movement of the liquid film. The mass conservation equation and the momentum conservation equation are both satisfied by the liquid film. When the liquid in the spray flow field comes into contact with the wall surface, its mass and momentum are added as source terms to the liquid film's mass and momentum conservation equations. The mass conservation equations are as follows:

$$(2.2) \qquad \frac{\partial h}{\partial t} + \nabla_s(h\,V_l) \;=\; \frac{\dot{m}_s}{\rho_l},$$

$$(2.3) \qquad \dot{m}_s \;=\; \alpha_d \rho_d V_{dn} A,$$

where $l$ represents the liquid film; $\rho_l$ is the density of the liquid film; $h$ is the height of the liquid film, $V_l$ is the average velocity of the liquid film, $\dot{m}_s$ is the mass source of unit wall area, $\alpha_d$ is the liquid volume fraction, $\rho_d$ is the liquid phase density, $V_{dn}$ is the velocity of the liquid phase perpendicular to the wall, and $A$ is the area of the wall. The momentum conservation equation is presented in (2.4). The left side of the momentum equation is transient and convection occurs. The action of air flow pressure and liquid film surface tension is represented by the first item on the right side of the equation, the action of viscous shear force at the air–liquid film interface is represented by the second item, the action of viscous force in the liquid film is represented by the third item, and the action of liquid film momentum source is represented by the fourth item. The momentum source $(\dot{q}_s)$ is given in Eq. (2.5)

$$(2.4) \qquad \frac{\partial h\,V_l}{\partial t} + \nabla_s \left( h\,V_l\,V_l \right) \;=\; -\frac{h\nabla_s\,P_l}{\rho_l} + \frac{3}{2\rho_l}\tau_{fs} + \frac{\dot{q}_s}{\rho_l},$$

$$(2.5) \qquad \dot{q}_s \;=\; \dot{m}_s V_d,$$

where $V_d$ is the liquid velocity.

## 2.3. Breakup models

The breakup model is one of the most significant sub-models that must be considered in the procedure of the atomization simulation. The spraying process is separated into two categories: primary and secondary breakup. In a primary breakup, due to the instabilities of the liquid film, droplets occur. The secondary breakup models explain the decomposition of the big droplets via normal stresses (instability of Rayleigh-Taylor) and also by stripping of the very small particles (instability of Kelvin-Helmholtz). The formulation and technique of the various breakup models are described in the following sections.

2.3.1. *TAB breakup model.* O'ROURKE and AMSDEN [15] developed the TAB model, which is regarded as one of the standard models for spray breakup estimates. The model is based on a spring-mass system and an oscillating and distorting droplet analogy. The surface tension forces are represented by the spring's restoring force, while the external force on the mass is the gas aerodynamic force, and the damping force is the liquid viscous effects. A damped, forced harmonic oscillator equation is as follows:

$$(2.6) \qquad F - kx - d\frac{\mathrm{d}x}{\mathrm{d}t} = m\frac{\mathrm{d}^2x}{\mathrm{d}t^2},$$

where $x$ denotes the displacement of the droplet's equator from its equilibrium location, $F$ is the external forces (equivalent to aerodynamic drag), $k$ is the

spring constant (related to surface tension), and $d$ is the damping parameter (corresponding to viscous forces). The physical dependencies of the coefficients according to the Taylor analogy are

$$(2.7) \qquad \frac{F}{m} = C_F \frac{\rho_g u^2}{\rho_l r},$$

$$(2.8) \qquad \frac{k}{m} = C_k \frac{\sigma}{\rho_l r^3},$$

$$(2.9) \qquad \frac{d}{m} = C_d \frac{\mu_l}{\rho_l r^2},$$

where $C_F$, $C_k$, and $C_d$ are dimensionless numbers. $C_b$ is used to non-dimensionalize $x$ by defining $y = x/(C_b r)$. Now, the equation of the oscillator can be written as:

$$(2.10) \qquad \frac{\mathrm{d}^2 y}{\mathrm{d}t^2} = \frac{C_F}{C_b} \frac{\rho_g u^2}{\rho_l r^2} - \frac{C_k \sigma}{\rho_l r^3} y - \frac{C_d \mu_l}{\rho_l r^2} \frac{\mathrm{d}y}{\mathrm{d}t}$$

with breakup occurring if and only if $y > 1$. Furthermore, it is assumed that breakup occurs if and only if the amplitude of oscillation of the north and south poles equals the droplet radius. The dimensionless constants $C_F$, $C_k$, and $C_d$ are determined by comparing them with experimental and theoretical results and have the following values, $C_k = 8$, $C_d = 5$, $C_k = 0.5$, and $C_F = 1/3$ [16].

### 2.3.2. *Kelvin-Helmholtz/Rayleigh-Taylor (KHRT) breakup model.*

The Kelvin-Helmholtz waves caused by aerodynamic forces are combined with Rayleigh-Taylor instabilities caused by shed drops expelled into freestream conditions in KHRT [17]. Both processes simulate droplet breakup by following the formation of waves on the droplet's surface, with breakup occurring due to the fastest-growing instability based on local conditions. The KHRT model implies the presence of a liquid core near the nozzle. When child droplets are ejected into the freestream from this liquid core, they are subjected to rapid acceleration, and Rayleigh-Taylor instability becomes the dominant effect. The Levich theory is used to calculate the length of the liquid core

$$(2.11) \qquad L = C_L d_o \sqrt{\frac{\rho_l}{\rho_g}},$$

where $C_L$ is the Levich constant, $d_o$ is a reference nozzle diameter, and $\rho_l$ and $\rho_g$ are the densities of liquid and gas, respectively. The Rayleigh-Taylor (RT)

model, like the Kelvin-Helmholtz model, is based on wave instabilities on the droplet surface. The frequency of the fastest-expanding wave is computed using

$$(2.12) \qquad \Omega_{\mathrm{RT}} = \sqrt{\frac{2\left(-g_t\left(\rho_g - \rho_P\right)\right)^{1.5}}{3\sqrt{3\sigma}\left(\rho_g + \rho_P\right)}},$$

where $g_t$ is the droplet acceleration in the droplet's travel direction. The wave number for the related wave is as follows:

$$(2.13) \qquad K_{\mathrm{RT}} = \sqrt{\frac{\left(-g_t\left(\rho_g - \rho_P\right)\right)}{3\sigma}}.$$

The breakup occurs when RT waves have grown for a longer period of time than the breakup time $\tau_{\mathrm{RT}}$ defined as:

$$(2.14) \qquad \tau_{\mathrm{RT}} = \frac{C_\tau}{\Omega_{\mathrm{RT}}}.$$

The Rayleigh-Taylor breakup time constant has a default value of 0.5. The wave growth is tracked when the predicted wavelength, corresponding to the fastest wave growth rate, is smaller than the local droplet diameter. The radius of the smaller child droplets is calculated with Eq. (2.15):

$$(2.15) \qquad r_c = \frac{2\pi C_{\mathrm{RT}}}{K_{\mathrm{RT}}},$$

where $C_{\mathrm{RT}}$ is the breakup radius constant, which has a value of 0.1 [18].

*2.3.3. Stochastic secondary droplet (SSD) model.* The SSD model [19] samples the secondary droplet size from an analytical solution of the Fokker-Planck equation for the probability distribution, and the probability of breakup is independent of the original droplet size. Furthermore, the size distribution characteristics are based on local conditions. According to the SSD model, a breakup occurs when a droplet exceeds a critical radius:

$$(2.16) \qquad r_c = \frac{\mathrm{We}_{\mathrm{cr}}\,\sigma_l}{\rho_g u_{\mathrm{rel}}^2},$$

where $\mathrm{We}_{\mathrm{cr}}$ is the critical Weber number. The default value of the critical Weber number is 6. The breakup time is defined as follows:

$$(2.17) \qquad t_{bu} = B\sqrt{\frac{\rho_l}{\rho_g}}\frac{r}{|u_{\mathrm{rel}}|},$$

where $u_{\mathrm{rel}}$ is the relative velocity between droplets and particles, and $B$ is the user-specified breakdown constant with a value of 1.73. The breakup occurs when the parcel's breakup time exceeds the critical breakup time.

## 3. Evaluation of atomization characteristics

The mean diameter $D_{j,k}$ can be used to evaluate droplet atomization, as indicated in Eq. (3.1)

$$(3.1) \qquad (D_{j,k})^{j-k} = \frac{\displaystyle\int_0^\infty D^j f(D)\,\mathrm{d}D}{\displaystyle\int_0^\infty D^k f(D)\,\mathrm{d}D},$$

where $f(D)$ is the droplet diameter distribution function, while $j$ and $k$ are integers. The mean diameter has several meanings depending on the values of $j$ and $k$. Table 1 provides some common mean diameter definitions.

**Table 1**. Common mean diameter definitions.

| Symbols | Name | Application area |
|---|---|---|
| $D_{1,0}$ | average diameter | evaporation |
| $D_{2,1}$ | average surface area diameter | absorption consolidation |
| $D_{3,0}$ | average volume diameter | hydrology |
| $D_{3,2}$ | Sauter mean diameter | combustion, atomization, mass transfer |
| $D_{4,3}$ | Debruk diameter | combustion balance |

The Sauter diameter $(D_{3,2})$, which is defined as the particle size of a hypothetical droplet group with the same particle shape, total volume, total surface area, and uniform particle size, that is, the diameter of a sphere with the same surface area as the actual atomized droplet, is the common index used to evaluate the atomization effect in the spray atomization process [20].

### 3.1. Comparison of different breakup models

Choosing an appropriate breakup model is a crucial issue in the spraying simulation because it determines the child droplet size and mass. The droplet size is a factor that has an important effect on their trajectory, overspray phenomenon, and the created film thickness on the target geometry. While other parameters are kept constant, three different breakup models and their effects on average particle diameter and particle mean velocities are compared and results are shown in Fig. 1. As it can be seen in the Fig. 1, KHRT produces bigger particles in diameter relative to SSD and TAB models.
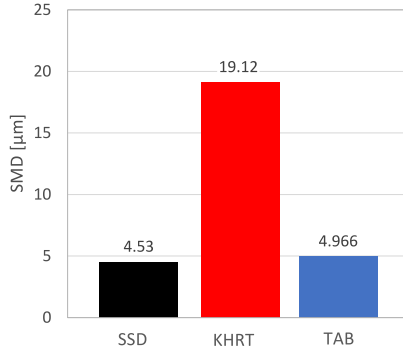
FIG. 1. Particle diameter distribution of different secondary breakup models.

## 4. MODEL DEFINITION AND ANALYSIS SETTINGS

### 4.1. Air assisted spray gun geometry

The 3D computer aided design (CAD) model of the air cap of an air-assisted spray gun is created in the SolidWorks software (2017).

Based on [11], the same geometry is used and shown in Fig. 2. Below the 26 mm paint hole, the origin point of the computational domain is inserted. The $x$-axis is parallel to the short axis of ellipse, the $y$-axis is parallel to the long axis of the ellipse, and the $z$-axis is parallel to the air-assisted spray gun axis.
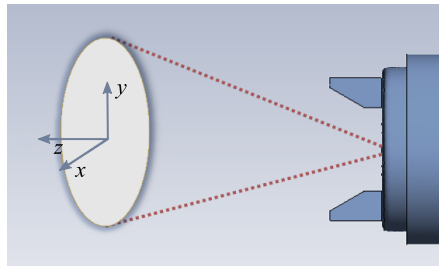


FIG. 2. Illustration of spray cone geometry.

There are four kinds of different holes, as shown in Fig. 3. From the coating hole, the coating material is sprayed. Atomizing air hole mainly helps to jet stream speed up and atomize the liquid. Assisting holes are mainly required to clean up the air cap surface. Shaping holes are required to expand and contract the spray flow field and cone geometry by increasing the inlet pressure when it is needed. In this work, there is a circular paint hole with a diameter of 1.5 mm, and an annular atomization hole surrounds the coating hole of 2.5 mm in diameter. There are four assisting air holes with a diameter of 0.5 mm on both
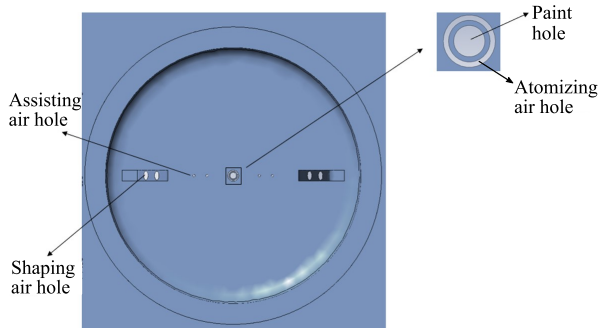
FIG. 3. The spray gun's air cap geometry.

sides of the air cap. There are four symmetric shaping air holes with a diameter of 2 mm on both sides of the air cap.

### 4.2. Numerical method and initial conditions

The simulation of 3D compressible flow, particle atomization, and film deposition on the target surface is done in this research using the commercial CFD program ANSYS-Fluent 2020 R2. The paint is atomized into tiny droplets by the high-pressure airflow. Under the influence of airflow, the droplets are carried onto the target surface, forming a coating film. As it can be seen in Fig. 4, the air cap is placed in such a way that the paint hole is 26 mm above the origin $(L^*)$, and the distance between the paint hole and the coating surface is 200 mm. An unstructured grid with tetrahedral and prism elements is used in this paper with the help of the Ansys Fluent meshing tool because it can better fit the complex geometry of the computational domain.
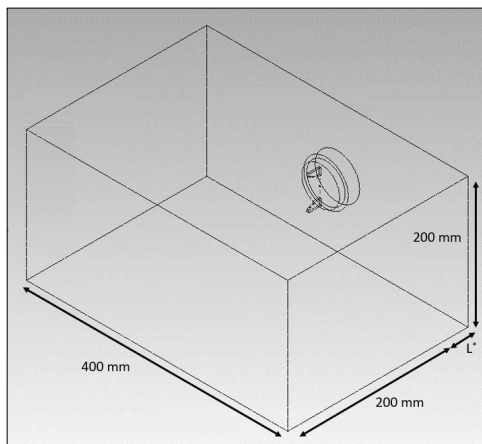


FIG. 4. Structure of the computational domain.

In order to assure calculation accuracy while reducing computer resource usage, a local grid refinement approach is adopted. To accurately model the interaction between air and droplets, the grid around the air spray gun is refined. To keep the total number of computing cells down, the region far away from the air spray gun has coarser elements. *X-Z* cross-sectional details of the mesh structure are shown in Fig. 5.
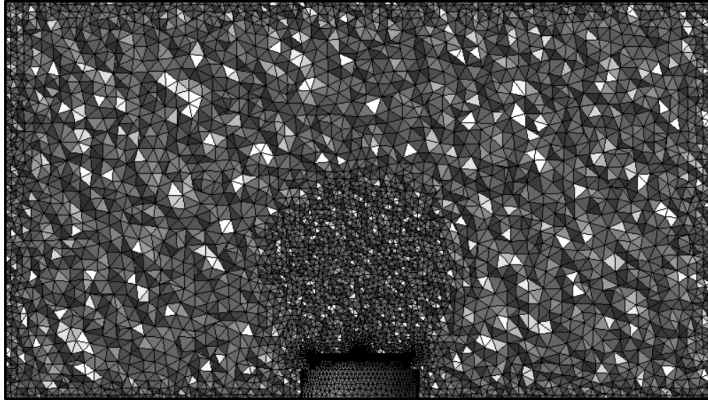


FIG. 5. *X-Z* cross-sectional view of the mesh structure.

In this paper, as inlet boundary conditions, all air vents except the paint hole are defined as pressure inlets. For the paint hole, the mass flow inlet boundary condition is selected by selecting the paint hole as the surface from the injections section. Droplets are directly injected using the face normal direction. The initial velocity of droplets is 5 m/s, with a mass flow rate of $1.5 \cdot 10^{-3}$ kg/s and density of $1.2 \cdot 10^{-3}$ kg/m$^3$. The total injection time is 1 s, and the injection starts at 0.06 s. The pressure outlet boundary condition is given, assuming all surfaces except the surface where the air cap geometry is located and the surface intended to be coated, are opened to the atmosphere (with a gauge pressure of 0 MPa). The coating surface is an adiabatic wall with no-slip boundary condition. A discrete phase boundary condition coating surface is set as "trap" and the other wall surfaces as "reflect". The inlet conditions of the air cap surfaces, materials' thermophysical properties, and injection parameters are summarized in Tables 2, 3, and 4, respectively.

**Table 2**. Air and coating material properties.

| Materials | Viscosity [Pa$\cdot$s] | Density [kg/m$^3$] | Surface tension [mN/m] |
|-----------|------------------------|--------------------|------------------------|
| Air | $1.8 \cdot 10^{-5}$ | 1.29 | – |
| Paint | 0.065 | 1200 | 71.9 |

**Table 3**. Simulation application parameters.

| Flow rate of liquid [kg/m$^3$] | Assisting air pressure [MPa] | Atomizing air pressure [MPa] | Shaping air pressure [MPa] |
|---|---|---|---|
| $15 \cdot 10^{-3}$ | 0.15 | 0.15–0.20–0.25 | 0.07 |

**Table 4**. Injection parameters.

| Diameter [μm] | Start time [s] | Stop time [s] | Velocity magnitude [m/s] |
|---|---|---|---|
| 65 | 0.06 | 1 | 5 |

At this point, according to a method that is widely used and directly related to the measurement, the diameter and velocity distributions of the particles can be obtained from a certain distance downstream of the nozzle (from a point where atomization is thought to have occurred completely), and these data can be injected into the discrete phase from a rectangular surface and the coating thickness on the target surface can be measured [10]. By this approach, the droplet breakup is bypassed, and solution accuracy may be affected. In this paper, the discrete phase is added at the inlet of the spraying hole so that the influence of gas flow on the movement of droplets can be fully considered. The TAB model is used to predict the secondary breakup and the child droplets' diameters. Since the TAB model is not intended to model the primary breakup, we have to set up a model that can be used as input to the TAB model. According to reference [11], droplets with an initial diameter of 65 μm are injected into the airflow at the position of the paint hole in this work. In the absence of an accurate model, this assumption is considered accurate.

## 5. NUMERICAL RESULTS AND DISCUSSION

### 5.1. Model validation and grid independency study

During the numerical simulation, the quality of the grid will affect the accuracy of the calculation. In addition, the finer the mesh elements, the longer the calculation time. In order to eliminate the effect of the number of cells on the calculation results and determine the optimal number of cells for calculation, the grid independence is studied.

In order to examine the effects of mesh density on the solution, four kinds of grids: 0.27, 0.535, 0.85, and 1 million are generated and compared with results from [11]. Figure 6 shows the results. As can be seen in this figure, distributions are quite comparable to each other. In this work, due to the limitations on the computational sources and by considering solution time, 530 000 elements are taken during the calculations. The orthogonal quality of the mesh is 0.76, and the skewness is 0.23. It is considered enough for spraying applications.
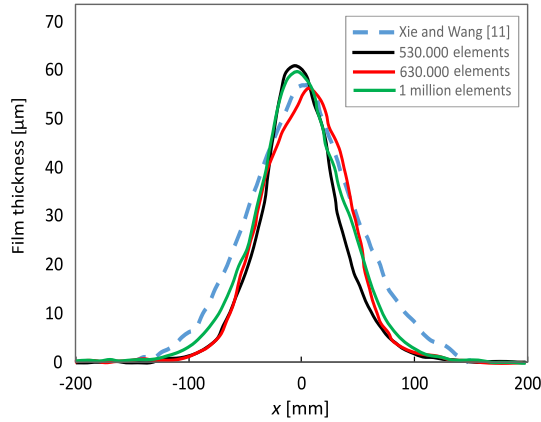
FIG. 6. Comparison of the film thickness distribution of grid elements: 0.53, 0.63, 1 million with XIE and WANG [11] along the $y$-axis.

## 5.2. Effect of average particle diameter and film height

For easier viewing of the whole film thickness on the target surface, the maximum visible film thickness is set to 40 μm. There is an intense coated region in the middle of the coating surface, which then decreases with distance from the center. Regardless of the width of the distribution, the coating thickness increases with decreasing particle size. A possible explanation is based on the ratio of the attractive forces between particles and the gravitational force acting upon the particles. This ratio increases with decreasing particle size. Larger droplets, because of their higher momentum, separate from the annular jet air stream. Moreover, with a narrower particle size distribution, the number of small particles in the coating and, thus, the ratio of attractive forces and gravitational force increase even more at small median particle sizes resulting in a higher coating thickness [22]. The simulation results are shown in Fig. 7.
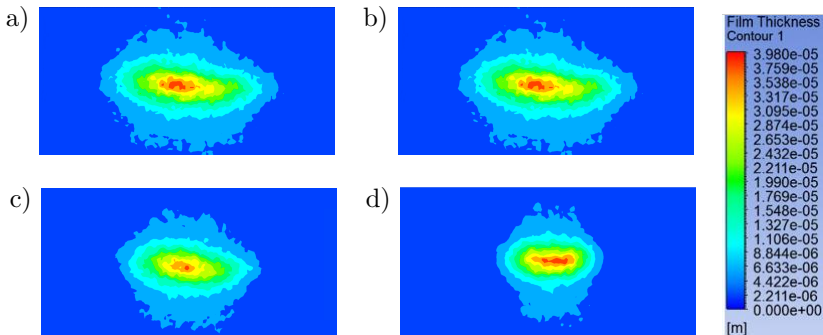


FIG. 7. Coating film thickness variation according to particle diameter:
a) $d = 65$ μm; b) $d = 40$ μm; c) $d = 20$ μm; d) $d = 10$ μm.

### 5.3. The effect of spraying distance on the uniformity of coating film shape and distribution

In order to better examine the effect of the spray distance on the film thickness and quality, 150 mm, 200 mm, and 300 mm distances are selected from the $L^*$ value and the coating distribution and integrity between the short edges of the target surface are examined. Figures 8 and 9 show the distribution of the coating material on the coating surface with the increase in spray height. It is found that the wet film thickness increases in the regions close to the center as the coating distance decreases. In this situation, the coating thickness at the center is too large to produce a hanging phenomenon, which is not sufficient to obtain better coating quality [23]. Also, the thickness at the edges decreases as the coating distance increases. This is because fragmented droplets leave the domain before reaching the target surface. The results are shown in Fig. 9.
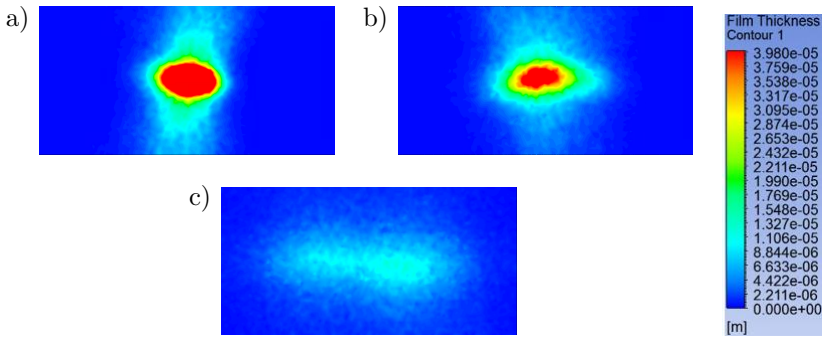


FIG. 8. Coating thickness distribution at different coating heights from $L^*$: a) $L = 150$ mm, b) $L = 200$ mm, c) $L = 300$ mm.
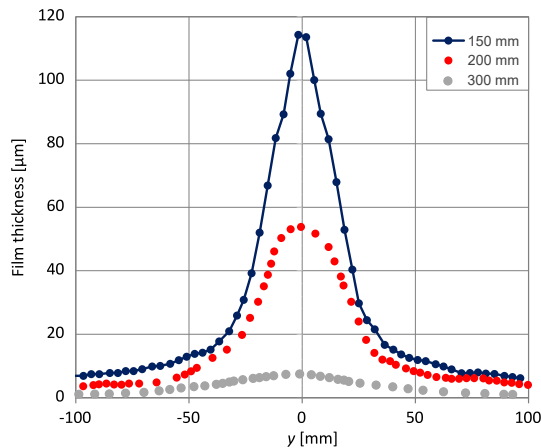


FIG. 9. Coating thickness distribution at different coating heights from $L^*$.

As shown in Figs. 10 and 11, the coating thickness between the long edges of the target coating surface is collected to form a fitting curve, and the curve of maximum coating thickness with spraying height is fitted to better examine the variation of coating thickness and distribution according to spraying distance. The coating thickness curve shows an uneven distribution with increasing spraying height, as seen in Fig. 10. The coating thickness in the center reduces dramatically when the spraying height exceeds 250 mm. The fundamental reason is that as the spraying height increases, the airfield has a greater impact on the droplet, altering the coating's homogeneity.
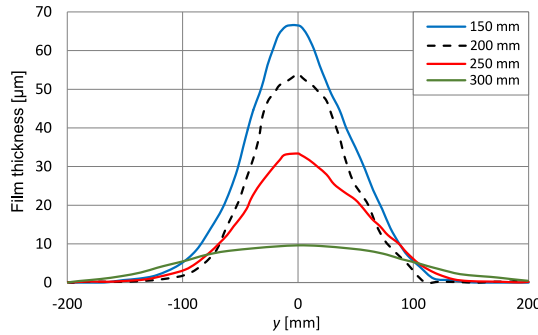
FIG. 10. Coating film thickness distributions from $L^*$.
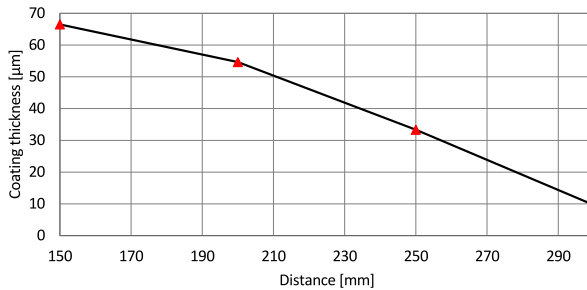
FIG. 11. Variation of the maximum coating thickness according to spraying height.

As can be observed in Fig. 11, the film thickness reduces as the spraying distance increases. After 200 mm, the coating thickness varies very little and then drops linearly.

## 5.4. Effects of atomizing air pressure on flow field and film thickness distribution

Three different atomizing air pressures are chosen to investigate the effect of atomizing air pressure on the airflow field, particle diameter distribution, and coating film thickness. The respective pressures are 0.15, 0.20, and 0.25 MPa.

The velocity contours along the long and short axis of atomizing air pressures are shown in Fig. 12. For easier viewing of the whole velocity field, the maximum visible velocity is set to 50 m/s. It is seen that the area near the spraying gun has higher airflow velocity, which gradually decreases in the $z$-axis direction.
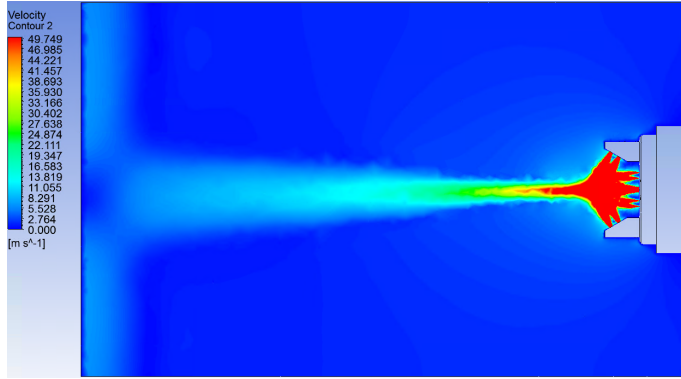


FIG. 12. Velocity contour of spray flow.

Figure 13 shows velocity vectors in the flow domain due to the different atomizing air pressures. It is clearly seen that around the nozzle, there is a su-
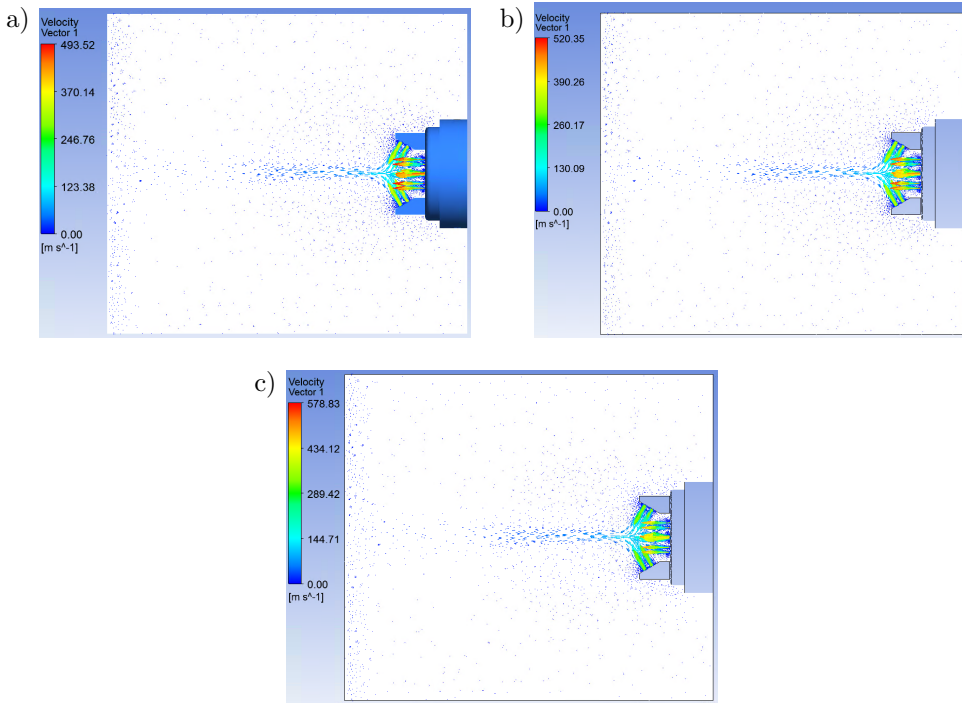


FIG. 13. Velocity contours of flow field: a) 0.15 MPa, b) 0.20 MPa, c) 0.25 MPa.

personic flow region due to high pressured airflow, which is drastically losing its velocity, and the flow becomes a subsonic flow as we move in the $z$-axis. Also, it is seen that as atomizing air pressure increases, the maximum visible velocity in the flow domain increases.

In this paper, in order to further examine the velocity profile along different distances in the $z$-direction, starting from the origin, different lines are assigned along the flow field in the $x$-$y$ axis, as shown in Fig. 14. The distances are $z = 50$ mm, $z = 65$ mm, $z = 80$ mm, $z = 95$ mm. Figure 15 depicts the velocity distribution for each z distance along the $x$-$y$ plane. Figure 15a shows that there
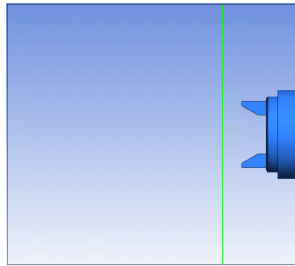


FIG. 14. Line assignment.
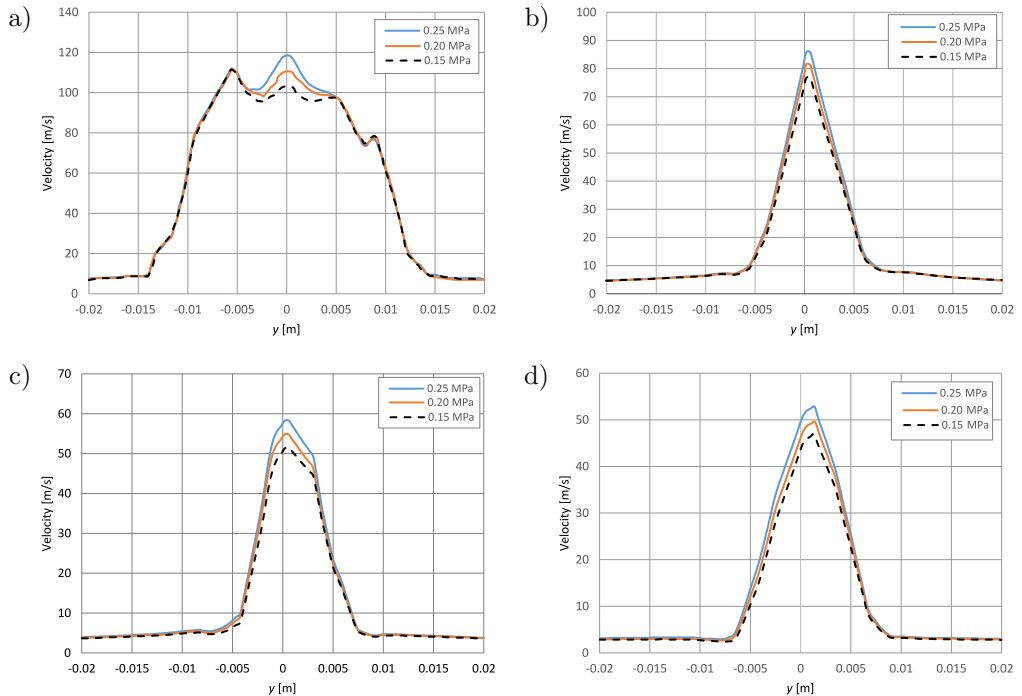


FIG. 15. Velocity distribution along the $z$-axis: a) $z = 50$ mm, b) $z = 65$ mm, c) $z = 80$ mm, d) $z = 95$ mm.

are different local and global peak values around the nozzle. Figures 15b–15d show that at the center of the flow field, the velocity is maximum, which shows Gaussian distribution. The peak values decrease gradually along the flow direction because of the consumption of momentum.

As expected, high pressures create smaller particles than low pressures throughout the whole spray cone due to increased momentum exchange and higher Re numbers. Figure 16 shows the coating distribution for different atomizing air pressures. It can be seen that whenever pressure is increased, smaller droplets create an intense region at the center of the target surface.
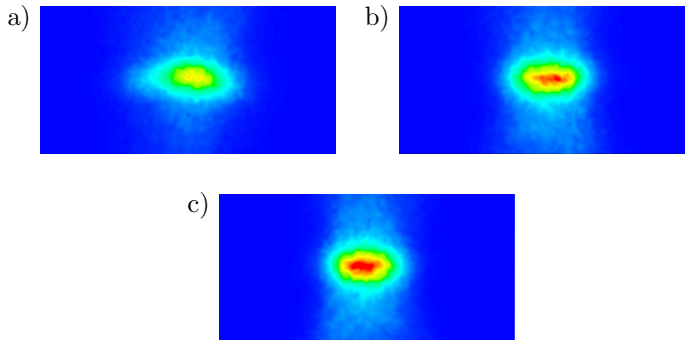


FIG. 16. Coating thickness distribution according to the atomizing air pressures: a) 0.15 MPa, b) 0.20 MPa, c) 0.25 MPa.

## 5.5. Effects of atomizing pressure on mean atomization speed and Sauter mean diameter

The average particle velocity is inversely related to particle diameter as: $V_p = k/dn$, where $V_p$ is the particle velocity, and $k$ and $n$ are the coefficients related to driving gas conditions for a certain material [24].

The velocity of the paint droplets affects the impact kinetic energy of the paint; therefore, it is necessary to analyze the velocity of the atomized particles. The impact kinetic energy is related to the impact strength of the paint on the wall; too much speed will increase the kinetic energy of the paint, resulting in the paint colliding with the outer hull plate and then splashing, thus reducing the deposition rate, resulting in waste of paint and environmental pollution problems. The relationship between the axial velocity of the paint and the spray distance of the paint particles under different pressure is shown in Fig. 17.

The SMD of particles at different atomizing air pressures is obtained by taking different pressure values between 0.15–0.55 MPa. As the pressure increases, the atomization diameter of the particles becomes smaller. As we approach the mean diameter of the droplets before the secondary breakup, all child droplets
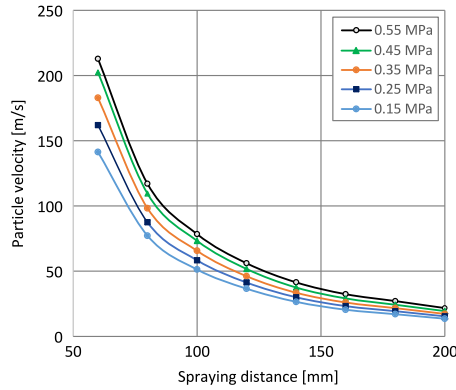
FIG. 17. Particle velocity changes according to the distance under different pressures.

have the same SMD over the $z$-axis. Figure 18 shows the relation between atomizing pressure and SMD change.
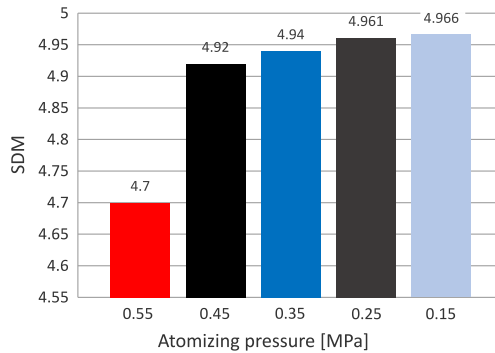


FIG. 18. SMD distribution for different pressures.

## 5.6. Effect of critical We number on particle velocity

Assuming different We numbers of 6, 12, 18, and 24 are used for simulation, the spraying simulation yields the spraying velocity of the paint particles under different critical We numbers, as shown in Fig. 19. The rapid velocity of the paint drops as much as 151 m/s near the nozzle. As the spraying distance increases, the droplets continue to exchange momentum with the air phase, and the velocity decreases to 15–20 m/s when it reaches the vicinity of the wall. The velocity decay of the particles is directly influenced by the critical We number of fragmentation. As can be seen, the larger the critical We number, the greater the particle velocity, and the more difficult the drops to atomize.
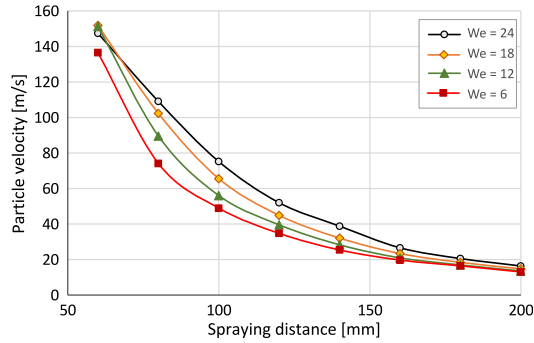
FIG. 19. Effects of critical We number on the particle velocity at different distances.

## 5.7. Experimental results

To confirm the applicability of the numerical method, the results from the CFD analysis are compared with the results from the experimental and numerical study in [11]. For this, the "planar vertical spraying" set up in the reference has been taken into account, the shaping air pressure is 0.07 MPa, and the total time is one second. As seen in Fig. 20, there is a good agreement between the numerical and experimental results.
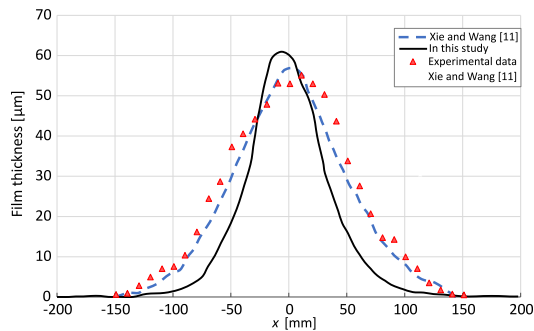


FIG. 20. Comparison of numerical results with the experimental results in [11].

## 6. CONCLUSION

In this article, we numerically examined the spray coating process with an air-assisted gun. A 3D model was generated to simulate the spraying flow and atomization process. Also a grid independency study was carried out to minimize solution time and useful consumption of the computational resources. In this sense, an unstructured type grid with 535 000 tetrahedrons was selected. To simulate a two-phase flow field, a coupled TAB-DPM model was used. The

DPM model was used for determining droplet trajectories and the TAB model was used to calculate child particle diameters.

The following results were obtained from the simulation of the effect of atomization pressure on atomized particle diameter, particle speed, and film thickness distribution.

As the coating height decreased, the dispersion was concentrated in the center of the coating surface and the coating thickness increased in the center. Conversely, as the spray distance increased, the coating deposits were smaller in the center and at the edges. Excessive coating thickness in the center can also cause extra thick areas on the products during the drying of the wet coating.

The larger the particle diameter, the less the film thickness. The middle of the coating zone is always thicker, and the thickness distribution of this region reduces as it moves out from the center. The ratio of the attractive forces between the particles and the gravitational force acting on the particles increases as particle size decreases. Larger droplets are separated from the circular jet airflow due to their increased momentum. Furthermore, with a smaller particle size distribution, the number of small particles in the coating increases even more at smaller particle sizes, leading to a high coating thickness.

The spraying flow field, child droplet sizes, and coating thickness on the target surface are all influenced by the atomizing air. The droplet sizes decrease as the atomizing air pressure increases, while the film coating thickness along the $y$-axis on the coating surface increases. Particle speed along the $y$-axis increases as atomizing air pressure increases. Spraying guns with high atomizing air pressures may thus improve spraying efficiency. However, if the atomizing air pressures are too high, over-spraying may occur.

The larger the critical Weber number, the greater the particle velocity, and the more difficult the drops to atomize. As the spraying distance increases, the droplets continue to exchange momentum with the air phase and the velocity decreases. The velocity decay of the particles is directly influenced by the critical We number of fragmentation. Particles with a higher We number have higher velocities.

## References

1. Antonio J.K., Optimal trajectory planning for spray coating, *Proceedings of the IEEE International Conference on Robotics and Automation*, vol. 3, pp. 2570–2577, 1994, doi: 10.1109/robot.1994.351125.

2. Ye Q., Domnick J., Analysis of droplet impingement of different atomizers used in spray coating processes, *Journal of Coatings Technology and Research*, **14**(2): 467–476, 2017, doi: 10.1007/s11998-016-9867-4.

3. Liao Y., Sakman A.T., Jeng S.M., Jog M.A., Benjamin M., A comprehensive model to predict simplex atomizer performance, *Proceedings of the ASME 1998 International Gas*

*Turbine and Aeroengine Congress and Exhibition. Volume 3: Coal, Biomass and Alternative Fuels; Combustion and Fuels; Oil and Gas Applications; Cycle Innovations*, Stockholm, Sweden, June 2–5, 1998, doi: 10.1115/98-GT-441.

4. ANSDELL D.A., Automotive paints, [in:] *Paint and Surface Coatings: Theory and Practice*, R. Lamboune, T.A. Strivens [Eds.], pp. 431–489, John Wiley & Sons, New York, NY, 1987.

5. CHEN H., XI N., SHENG W., DAHL J., Optimizing material distribution for tool trajectory generation in surface manufacturing, *Proceedings of the 2005 IEEE/ASME International Conference on Advanced Intelligent Mechatronics*, Monterey, CA, USA, pp. 1389–1394, 2005, doi: 10.1109/AIM.2005.1511205.

6. KIM D., YOON Y., HWANG S., LEE G., PARK J., Visualizing spray paint deposition in VR training, *Proceedings of 2007 IEEE Virtual Reality Conference*, Charlotte, NC, USA, pp. 307–308, 2007, doi: 10.1109/VR.2007.352515.

7. LUANGKULARB S., PROMBANPONG S., TANGWARODOMNUKUN V., Material consumption and dry film thickness in spray coating process, *Procedia CIRP*, **17**: 789–794, 2014, doi: 10.1016/j.procir.2014.02.046.

8. FOGLIATI M., FONTANA D., GARBERO M., VANNI M., BALDI G., DONDÈ R., CFD simulation of paint deposition in an air spray process, *JCT Research*, **3**(2): 117–125, 2006, doi: 10.1007/s11998-006-0014-5.

9. YE Q., DOMNICK J., KHALIFA E., Simulation of the spray coating process using a pneumatic atomizer, *ILLAS-EUROPE 2002, 18th Annual Conference on Liquid Atomization & Spray Systems*, Zaragoza, SPAIN, September, 9–11, 2002.

10. YE Q., SHEN B., TIEDJE O., BAUERNHANSL T., DOMNICK J., Numerical and experimental study of spray coating using air-assisted high-pressure atomizers, *Atomization and Sprays*, **25**(8): 643–656, 2015, doi: 10.1615/AtomizSpr.2015010791.

11. XIE X., WANG Y., Research on distribution properties of coating film thickness from air spraying gun-based on numerical simulation, *Coatings*, **9**(11): 721, 2019, doi: 10.3390/coatings9110721.

12. WANG Y.-A., XIE X.-P., LU X.-H., Design of a double-nozzle air spray gun and numerical research in the interference spray flow field, *Coatings*, **10**(5): 475, 2020, doi: 10.3390/coatings10050475.

13. HILTUNEN K. *et al.*, *Multiphase Flow Dynamics*, *Theory and Numerics*, VTT Publications 722, 2009.

14. ISHII M., Thermo-fluid dynamic theory of two-phase flow, *NASA STI/Recon Technical Report A*, **75**: 29657, 1975.

15. O'ROURKE P.J., AMSDEN A., The TAB method for numerical calculation of spray droplet breakup, *SAE Technical Paper*, No. 872089, 1987, doi: 10.4271/872089.

16. LAMB H., *Hydrodynamics*, 6th ed., Dover Publications, New York, 1945.

17. BEALE J.C., REITZ R.D., Modeling spray atomization with the Kelvin-Helmholtz/Rayleigh-Taylor hybrid model, *Atomization and Sprays*, **9**(6): 623–650, 1999, doi: 10.1615/AtomizSpr.v9.i6.40.

18. ANSYS Fluent Theory Guide, Ansys Inc., USA, 15317, pp. 724–746, 2020.

19. APTE S.V., GOROKHOVSKI M., MOIN P., LES of atomizing spray with stochastic modeling of secondary breakup, *International Journal of Multiphase Flow*, **29**(9): 1503–1522, 2003, doi: 10.1016/S0301-9322(03)00111-3.

20. YI Z., MI S., TONG T., LI K., FENG B., LI B., LIN Y., Simulation analysis on the jet flow field of a single nozzle spraying for a large ship outer panel coating robot, *Coatings*, **12**(3): 369, 2022, doi: 10.3390/coatings12030369.

21. LI W., QIAN L., SONG S., ZHONG X., Numerical study on the influence of shaping air holes on atomization performance in pneumatic atomizers, *Coatings*, **9**(7): 410, 2019, doi: 10.3390/coatings9070410.

22. BARTH N., SCHILDE C., KWADE A., Influence of particle size distribution on micromechanical properties of thin nanoparticulate coatings, *Physics Procedia*, **40**: 9–18, 2013, doi: 10.1016/j.phpro.2012.12.002.

23. LIU Y., ZENG Y., ZHAO X., LIU J., LIU D., Analysis of film forming law and characteristics for an air static spray with a variable position of the plane, *Coatings*, **11**(10): 1236, 2021, doi: 10.3390/coatings11101236.

24. LI C.-J., LI W.-Y., WANG Y.-Y., YANG G.-J., FUKANUMA H., A theoretical model for prediction of deposition efficiency in cold spraying, *Thin Solid Films*, **489**(1–2): 79–85, 2005, doi: 10.1016/j.tsf.2005.05.002.